COMPUTATIONAL MECHANICS
WCCM VI in conjunction with APCOM'04, *Sept. 5-10, Beijing, China*

Upscaling Technique for the Atomistic-Continuum Simulation of Shape Memory Alloys with the EAM Potential

Marcel Arndt[1]*

[1]*Institute for Numerical Simulation, University of Bonn, Wegelerstr. 6, 53115 Bonn, Germany*
e-mail: arndt@ins.uni-bonn.de, www: http://www.ins.uni-bonn.de

Abstract. In this paper the upscaling process for the passage from atomistic to continuum mechanical models of shape memory alloys is considered. First the modeling on the atomistic level is reviewed and a numerical simulation of a $Ni_{64}Al_{36}$ alloy is presented. Then the upscaling to an intermediate continuum mechanical model is performed by means of the inner expansion technique. This model is further approximated to extract the essential properties. The resulting continuum mechanical model is finally used for the numerical simulation of a SMA-based two-way micro-actuator.

Key words. Upscaling, multiscale simulation, continuum limit, quasi-continuum approximation, shape memory alloy.

1 Introduction

Many materials exhibit a complex behavior which needs to be resolved on different length scales. Macroscopic effects can often be well described by models on the continuum mechanical level, whereas for microscopical effects the atomistic level with the method of Molecular Dynamics (MD) is appropriate. Sometimes it is even necessary to take quantum mechanical effects into account for an accurate description of the microscale. The computation of the behavior on a coarse length scale usually cannot be done on a finer length scale due to computational limits. This shows the need of advanced analytical and numerical techniques to bridge the gap between the different scales.
Basically two different approaches exist to address this problem. First, techniques to combine two or more different length scales into one model are developed. Without any ambitions for completeness, let us mention the recent development of multiscale simulations and bridging techniques by E and Engquist [8], Tadmor, Ortiz and Philips [17] and Wagner and Liu [19]. On the other hand, models on a coarse length scale can be obtained from models on a fine length scale. This process is called upscaling. Here, as many fine-scale properties as possible should be retained in the coarse-scale model. Among known upscaling techniques let us mention the scaling technique which is used by Blanc, Le Bris and Lions [4], E and Huang [9] and others, the direct expansion technique which originates from Kruskal and Zabusky [12, 20] and the inner expansion technique by A. and Griebel [2, 3].
In this paper the relation between the atomistic and the continuum length scale is examined. First, the modeling on the atomistic level is shortly described. As an application, we present the results of the numerical simulation of a Ni-Al alloy. The potential energy for this alloy is given by the Embedded-Atom Method [7]. This material is especially interesting because it exhibits the shape memory effect. It belongs to the class of so-called smart materials and has many applications in the fields of medicine, engineering and nanotechnology.
We then come to the upscaling process to the continuum mechanical level. First, we use the inner expansion technique which was proposed by A. and Griebel in [2, 3] to derive an intermediate continuum model from the atomistic model. The technique is based on an expansion of the macroscopic deformation function y and leads to a description of the potential energy in terms of the derivatives of y up to a given order. It allows for an accurate description of the material properties.

In a second step, the intermediate continuum mechanical model is further approximated by extracting certain properties such as the Young modulus and the position of the wells. This way an effective continuum mechanical model is obtained. It is easier to use for numerical computations, but still retains the important physical properties.
Finally, the numerical implementation of the continuum model by finite elements is discussed. As an application, the dynamics of a two-way micro-actuator is simulated. Such devices can cause small and precise movements and play an important role in the rapidly advancing field of nanotechnology.

2 Atomistic Length Scale

2.1 Atomistic Model of Crystalline Solids

On the atomistic length scale, the specimen under consideration is described by a system of N interacting atoms. The atom positions are denoted by

$$\{y(x)\}_{x\in\mathcal{L}\cap\Omega}. \tag{1}$$

Here, the set $\mathcal{L}\cap\Omega$ serves as the reference configuration, where $\Omega\subset\mathbb{R}^d$ describes the form of the crystal and $\mathcal{L}$ is a lattice. The latter is given by the infinite periodic continuation

$$\mathcal{L} := \{x+Az \mid x\in\mathcal{L}_{\text{cell}}, z\in\mathbb{Z}^d\} \tag{2}$$

of the finite base cell $\mathcal{L}_{\text{cell}}\subset\mathbb{R}^d$ along the column vectors of the matrix $A\in\mathrm{GL}(d,\mathbb{R})$. Here $d\in\mathbb{N}$ denotes the spatial dimension. The function

$$y : \mathcal{L}\cap\Omega\to\mathbb{R}^d \tag{3}$$

describes the deformation from the reference configuration of the crystal in space. The behavior of the specimen is determined by the potential energy function $\Phi^{(\mathrm{A})}$. It depends on the atom positions:

$$\Phi^{(\mathrm{A})} = \Phi^{(\mathrm{A})}(\{y(x)\}_{x\in\mathcal{L}\cap\Omega}). \tag{4}$$

The time evolution of the atomistic system is governed by Newton's second law of motion

$$m\frac{\partial^2}{\partial t^2}y(x) = -\nabla_{y(x)}\Phi^{(\mathrm{A})}(\{y(\tilde{x})\}_{\tilde{x}\in\mathcal{L}\cap\Omega}) \qquad \forall x\in\mathcal{L}\cap\Omega, \tag{5}$$

where m denotes the mass of an atom.

2.2 Embedded-Atom Method

The potential energy $\Phi^{(\mathrm{A})}$ reflects the specific behavior of the material. A huge amount of different potentials for different materials has been proposed in the literature. The potential we use here for the Ni-Al alloy is given by the Embedded-Atom Method (EAM). It has been proposed by Daw and Baskes [7] and is widely used for the description of metals.
The EAM is based on the hypothesis that every potential induces a certain electron density. Vice versa, it has been shown by Hohenberg and Kohn [10] that the electron density uniquely determines the potential. This principle is employed by the EAM to define the potential in terms of the electron density. Every atom $x\in\mathcal{L}\cap\Omega$ is embedded in the set of surrounding atoms, the so-called host. The electron density of the atom is then assumed to depend on the electron density ρ_x^{host} of the host:

$$\Phi_x^{\text{emb}} = F_x\big(\rho_x^{\text{host}}\big). \tag{6}$$

The embedding function F_x is fitted to the material properties. We furthermore assume that ρ_x^{host} is given by the superposition of the electron densities of the single atoms in the host. The latter are presumed to be

radially symmetric functions of the distance. They depend on the type of the atom and are quantified by single-determinant Hartree-Fock calculations, see [5]. Thus we write

$$\rho_x^{\text{host}} = \sum_{\tilde{x} \in \mathcal{L} \cap \Omega} \rho_{\tilde{x}}^{\text{atom}}(\|y(x) - y(\tilde{x})\|). \tag{7}$$

Hence the embedding part of the overall potential is given by

$$\Phi^{\text{emb}} = \sum_{x \in \mathcal{L} \cap \Omega} \Phi_x^{\text{emb}} = \sum_{x \in \mathcal{L} \cap \Omega} F_x \left(\sum_{\tilde{x} \in \mathcal{L} \cap \Omega} \rho_{\tilde{x}}^{\text{atom}}(\|y(x) - y(\tilde{x})\|) \right). \tag{8}$$

Note that Φ^{emb} is not a pair potential, because F_x is nonlinear in general.
The embedding part by itself is not sufficient to describe the physical properties of the solid.[1] Therefore we augment it by a pair potential

$$\Phi_x^{\text{pair}} = \frac{1}{2} \sum_{\tilde{x} \in \mathcal{L} \cap \Omega} \frac{Z_x(\|y(x) - y(\tilde{x})\|) Z_{\tilde{x}}(\|y(x) - y(\tilde{x})\|)}{\|y(x) - y(\tilde{x})\|}. \tag{9}$$

The functions Z_x and $Z_{\tilde{x}}$ can be interpreted as effective charges. They vanish for distances of more than a few Å. The pair potential can thus be interpreted as a localized Coulomb potential.
All in all the potential energy is given by

$$\Phi^{(\text{A})} = \Phi^{\text{emb}} + \Phi^{\text{pair}} = \sum_{x \in \mathcal{L} \cap \Omega} \Phi_x^{\text{emb}} + \Phi_x^{\text{pair}}. \tag{10}$$

2.3 Atomistic Simulation of a Ni-Al Alloy

Now we employ the EAM potential to simulate a $Ni_{64}Al_{36}$ shape memory alloy on the atomistic level. The concrete material parameters for the EAM potential have been taken from [11].
At higher temperatures, the lattice of the specimen has the B2 structure, see e.g. [16]. One cubic sublattice only consists of Ni atoms, whereas the other one is randomly occupied by Ni and Al atoms. This reflects the composition of a real Ni-Al alloy. The reference configuration is chosen as a ball of 2474 atoms arranged in this structure. The choice of a ball instead of a cube reduces the boundary effects.
Next we perform a molecular dynamics simulation of the time evolution of this system as governed by equation (5). To this end, the reference configuration is taken as the initial configuration. The initial velocities of the atoms are chosen randomly to realize the initial temperature of 800K. Additionally the system is subjected to a cooling process from 800K to 100K during the simulation. This is achieved by scaling the atom velocities by a uniform factor. The system of ordinary differential equations (5) is discretized in time by means of the leap-frog scheme. The resulting system is then numerically integrated.
Figure 1 shows four snapshots of the solution. The Ni atoms are plotted in blue and the Al atoms in green. The upper left snapshot shows the initial configuration. The B2 lattice structure can be clearly recognized here. Shortly after this, the atoms undergo a slight perturbation due to the temperature, but the lattice structure remains intact, see the upper right snapshot. But as the cooling proceeds, the systems undergoes a martensitic structural transformation. The body-centered B2 lattice is transformed to a tetragonal face-centered lattice (fct). The beginning of the transformation is shown in the lower left snapshot. The last snapshot shows the system at the final temperature of 100K. Here the phase transformation is fully finished. The system has been transformed from the austenitic phase at high temperature to the martensitic phase at low temperature. Note that the crystal did not only change its lattice structure, but also underwent a macroscopic deformation. It has been elongated along one axis (the x-axis in the figure), whereas it has been compressed along the other two axes. This transformed the ball into an ellipsoid. We will come back to this later.

[1] The Young modulus of the embedding part fulfills the relation $C_{44} = 0$ and $C_{11} = C_{12}$, which is violated by measurements of real solids.

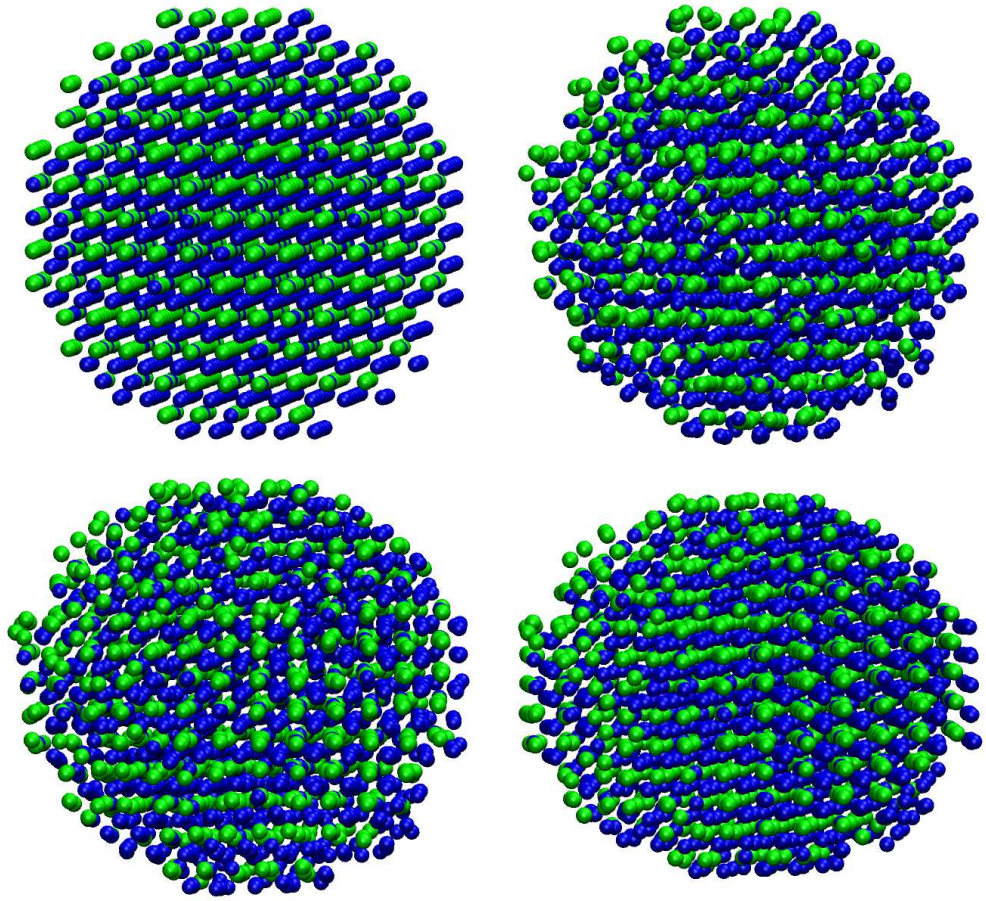

Figure 1: Snapshots of molecular dynamics simulation of $Ni_{64}Al_{36}$.

3 Inner Expansion Technique

After we studied the crystal on the atomistic level, we now come to the upscaling to the continuum mechanical level. Several techniques exist to perform the upscaling process, such as the scaling technique, see e.g. [4] and [9], and the direct expansion technique, see e.g. [12], [20], [6], [13] and [14]. Here we use the inner expansion technique which has been proposed by A. and Griebel in [2] and [3] to derive a quasi-continuum model. In the following we briefly describe the scheme. For details we refer to the mentioned papers.
First we split the overall potentials in the sum of local potentials around some center points $\overline{x} \in \overline{\mathcal{L}} \cap \Omega$, where $\overline{\mathcal{L}}$ denotes an associated lattice. In case of the EAM potential (10), the splitting is already given by the two sums. The points $\overline{x}$ are simply chosen as the points x for the embedding part and as the center points $\overline{x} = \frac{1}{2}(x+\tilde{x})$ for the pair interaction part. This leads to a description of the potential in the form

$$\Phi^{(\mathrm{A})}(\{y(x)\}_{x\in\mathcal{L}\cap\Omega}) = \sum_{\overline{x}\in\overline{\mathcal{L}}\cap\Omega} \Phi^{(\mathrm{A}),\overline{x}}(\{y(x)\}_{x\in\mathcal{L}\cap\Omega}). \tag{11}$$

Up to now, the deformation function y is defined only discretely on the finite set $\Omega \cap \mathcal{L}$, cf. (3). For the upscaling, an energy has to be assigned to a deformation function $y : \Omega \to \mathbb{R}^d$ which is continuously defined on the whole domain $\Omega \subset \mathbb{R}^d$. To this end, we consider the Taylor expansion of y around the point $\overline{x} \in \overline{\mathcal{L}} \cap \Omega$ up to some degree $K \in \mathbb{N}$:

$$y(x) \approx \sum_{k=0}^{K} \frac{1}{k!} \nabla^k y(\overline{x}) : (x-\overline{x})^k. \tag{12}$$

The colon is a short notation for the higher dimensional scalar products. The expression (12) now allows to

rewrite the local potential $\Phi^{(\mathrm{A}),\bar{x}}$ as follows:

$$\Phi^{(\mathrm{A}),\bar{x}}(\{y(x)\}_{x\in\mathcal{L}\cap\Omega}) \approx \Phi^{(\mathrm{A}),\bar{x}}\left(\left\{\sum_{k=0}^{K}\frac{1}{k!}\nabla^k y(\bar{x}) : (x-\bar{x})^k\right\}_{x\in\mathcal{L}\cap\Omega}\right)$$
$$= \Phi^{(\mathrm{I}),\bar{x}}(y(\bar{x}),\nabla y(\bar{x}),\nabla^2 y(\bar{x}),\ldots,\nabla^K y(\bar{x})). \tag{13}$$

Here $\Phi^{(\mathrm{I}),\bar{x}}$ is defined by

$$\Phi^{(\mathrm{I}),\bar{x}}(d_0,d_1,d_2,\ldots,d_K) := \Phi^{(\mathrm{A}),\bar{x}}\left(\left\{\sum_{k=0}^{K}\frac{1}{k!}d_k : (x-\bar{x})^k\right\}_{x\in\mathcal{L}\cap\Omega}\right). \tag{14}$$

Thus we transformed the original potential $\Phi^{(\mathrm{A}),\bar{x}}$, which depends on the deformation function y at all lattice points $x\in\mathcal{L}\cap\Omega$, to a representation which depends on the derivatives of y, evaluated only at the single point $\bar{x}$. The overall potential $\Phi^{(\mathrm{I})}$ is now given by

$$\Phi^{(\mathrm{I})}(y) = \sum_{\bar{x}\in\overline{\mathcal{L}}\cap\Omega}\Phi^{(\mathrm{I}),\bar{x}}\left(y(\bar{x}),\nabla y(\bar{x}),\nabla^2 y(\bar{x}),\ldots,\nabla^K y(\bar{x})\right). \tag{15}$$

This representation of the potential energy still contains the finite sum over all expansion points $\bar{x}\in\overline{\mathcal{L}}\cap\Omega$. Note that this sum is a Riemann sum, which is close to an integral. Therefore it makes sense to average it by passing to the integral representation

$$\Phi^{(\mathrm{J})}(y) = \frac{1}{|\det A|}\int_\Omega \Phi^{(\mathrm{I}),\bar{x}}\left(y(\bar{x}),\nabla y(\bar{x}),\nabla^2 y(\bar{x}),\ldots,\nabla^K y(\bar{x})\right)\,\mathrm{d}\bar{x}. \tag{16}$$

The factor $\frac{1}{|\det A|}$ stems from the volume of the base cell of the lattice, c.f. (2). We emphasize that the transition to the integral does not correspond to letting the number N of atoms tend to infinity like the scaling technique does. Instead, it is still an approximated description of the system for a fixed finite number N of atoms. Thus we call it an approximation within the quasi-continuum regime.
This technique is applied to the EAM potential in a straightforward but tedious calculation. The resulting terms are long and intricate, hence we do not state them here.

4 Macroscopic Approximation

The continuum mechanical model which is achieved in the last section can now be used to simulate the Ni-Al alloy on the continuum mechanical level. However, this is computationally expensive due to the complexity of the terms. Therefore we perform a next step of approximation on the macroscopic level to extract the essential properties.

4.1 Macroscopic Approximation of the Principal Part

To study the phase transformation process, it suffices to restrict ourselves to the principal part ∇y of the approximation. Therefore we choose the order $K=1$ of approximation for the inner expansion technique in Section 3. We yield the continuum mechanical energy

$$\Phi^{(\mathrm{J})}(y) = \int_\Omega \Phi^{(\mathrm{I}),\bar{x}}(y(\bar{x}),\nabla y(\bar{x}))\,\mathrm{d}\bar{x}. \tag{17}$$

For the EAM potential, the energy density $\Phi^{(\mathrm{I}),\bar{x}}$ is homogeneous, i.e. it does not depend on $\bar{x}$. Furthermore the translational invariance of the potential allows to skip the dependence on y. Therefore we shortly write

$$\Phi^{(\mathrm{J})}(y) = \int_\Omega \varphi(\nabla y(\bar{x}))\,\mathrm{d}\bar{x}. \tag{18}$$

Representative W	Number of occurrence
$W_1 = \begin{pmatrix} 1.2256 & 0 & 0 \\ 0 & 0.89522 & 0 \\ 0 & 0 & 0.89522 \end{pmatrix}$	658.673
$W_2 = \begin{pmatrix} 0.89522 & 0 & 0 \\ 0 & 1.2256 & 0 \\ 0 & 0 & 0.89522 \end{pmatrix}$	654.655
$W_3 = \begin{pmatrix} 0.89522 & 0 & 0 \\ 0 & 0.89522 & 0 \\ 0 & 0 & 1.2256 \end{pmatrix}$	654.786
unattainable	31.886

Table 1: Normal form of the minima of the potential energy.

Each mechanical system tends to minimize the potential energy. For the time evolution of such systems, this is expressed by Newton's second law of motion, which states that the acceleration always points towards the direction of steepest descent of the potential energy. In the stationary setting, the minimization of the potential energy is even imposed as the governing principle. Consequently, the system stays nearby of the minima of the energy landscape. Thus it makes sense to approximate the energy landscape in the vicinity of the minima.

First, the minima of the potential energy have to be identified. Since there are infinitely many of them, a classification is in order. To this end, we employ the invariance of the atomistic potential with respect to rigid body motions. It has been shown in [1] that the invariance also transfers to the continuum mechanical level. Thus φ is frame indifferent, i.e. we have $\varphi(\nabla y) = \varphi(R\nabla y)$ for all orthogonal matrices $R \in O(d)$. The set of all minima therefore is the union of several so-called wells $O(d)W$. The polar decomposition lemma states that each well contains exactly one representative which is symmetric positive definite. This turns out to be a convenient normal form for W.

Therefore our task is to identify the representative W of each well. For this purpose, a Monte Carlo technique is carried out to scan the region of attainable deformations. Each such deformation is used as a starting point for a minimization routine. Here a steepest-descent minimization technique with an Armijo step-size control is employed. This ensures that the set of all possible minima is detected. For each minimum which is found this way the according representative is determined by means of the polar decomposition. The whole process has been performed 2.000.000 times. The results are given in Table 1. A few minima have to be removed because the algorithm converged to a non-attainable minimum. Note that the elongation along one axis and the compression along the other two axes which is expressed by the wells has already been observed in the atomistic simulation.

The wells W_1, W_2 and W_3 correspond to the martensitic phase. The austenitic phase cannot be found by the same technique, because the potential describes the crystal at zero temperature at which the austenitic phase does not occur. Since we have chosen the reference configuration such that it corresponds to the austenitic phase, we add the well $W_0 = I$. Thus we deal with four wells W_0, W_1, W_2 and W_3.

Secondly, we approximate the energy density φ in the vicinity of the wells. To reduce the degrees of freedom, we employ the polar decomposition lemma once more. It states that each frame indifferent function φ can be expressed in terms of the strain tensor. The latter is given by

$$\varepsilon^i = \frac{1}{2}(W_i^{-T}\nabla y^T \nabla y W_i^{-1} - I), \tag{19}$$

relative to the well W_i. Hence we have

$$\varphi(\nabla y) = \hat{\varphi}_i(\varepsilon^i). \tag{20}$$

Well W_1	Well W_2	Well W_3	Value
$\mathbb{C}^1_{1111} =$	$\mathbb{C}^2_{2222} =$	$\mathbb{C}^3_{3333} =$	553.119 GPa
$\mathbb{C}^1_{2222} = \mathbb{C}^1_{3333} = \mathbb{C}^2_{1111} = \mathbb{C}^2_{3333} = \mathbb{C}^3_{1111} = \mathbb{C}^3_{2222} =$			491.451 GPa
$\mathbb{C}^1_{2233} =$	$\mathbb{C}^2_{1133} =$	$\mathbb{C}^3_{1122} =$	292.370 GPa
$\mathbb{C}^1_{1122} = \mathbb{C}^1_{1133} = \mathbb{C}^2_{1122} = \mathbb{C}^2_{2233} = \mathbb{C}^3_{1133} = \mathbb{C}^3_{2233} =$			412.757 GPa
$\mathbb{C}^1_{2323} =$	$\mathbb{C}^2_{1313} =$	$\mathbb{C}^3_{1212} =$	44.720 GPa
$\mathbb{C}^1_{1212} = \mathbb{C}^1_{1313} = \mathbb{C}^2_{1212} = \mathbb{C}^2_{2323} = \mathbb{C}^3_{1313} = \mathbb{C}^3_{2323} =$			104.353 GPa

Table 2: Young modulus of the martensitic wells W_1, W_2 and W_3. All remaining constants vanish.

Well W_0
$\mathbb{C}^0_{1111} = \mathbb{C}^0_{2222} = \mathbb{C}^0_{3333} =$ 472.443 GPa
$\mathbb{C}^0_{1122} = \mathbb{C}^0_{1133} = \mathbb{C}^0_{2233} =$ 389.630 GPa
$\mathbb{C}^0_{1212} = \mathbb{C}^0_{1313} = \mathbb{C}^0_{2323} =$ 102.724 GPa

Table 3: Young modulus of the austenitic well W_0. All remaining constants vanish.

We perform the Taylor expansion of $\hat{\varphi}_i$ around the minimum $\varepsilon^i = 0$:

$$\hat{\varphi}_i(\varepsilon_i) \approx \hat{\varphi}_i(0) + \sum_{kl} \frac{\partial \hat{\varphi}_i}{\partial \varepsilon^i_{kl}}\Big|_{\varepsilon^i=0} \varepsilon^i_{kl} + \frac{1}{2} \sum_{klmn} \frac{\partial^2 \hat{\varphi}_i}{\partial \varepsilon^i_{kl} \partial \varepsilon^i_{mn}}\Big|_{\varepsilon^i=0} \varepsilon^i_{kl} \varepsilon^i_{mn}. \tag{21}$$

The first order derivatives $\frac{\partial \hat{\varphi}_i}{\partial \varepsilon^i}\big|_{\varepsilon^i=0}$ vanish because we are in a local minimum. The second order derivative $\frac{\partial^2 \hat{\varphi}_i}{\partial {\varepsilon^i}^2}\big|_{\varepsilon^i=0} =: \mathbb{C}^i$ is called the Young modulus. Due to the symmetry of the strain tensor ε^i, there can be only 21 different values at maximum, compared to 81 values for an expansion of φ in terms of ∇y. In our case of the EAM potential, the Young modulus of the martensite computes to the values given in Table 2. Note that several values coincide due to the tetragonal symmetry of the martensitic wells.
We cannot proceed similarly for the austenite, because φ describes the energy at zero temperature, at which only the martensite phase does exist. As a remedy, we transform the Young modulus of the martensite, which is relative to the well W_i, back to W_0 and adapt it to the cubic symmetry group, see [1] for details. This leads to the values stated in Table 3.
It remains to determine the constants $\hat{\varphi}_i(0)$, which describe the offset of the potential energy for the respective wells. They are assumed to depend linearly on the temperature. The difference between the martensitic and the austenitic offset is given by

$$\hat{\varphi}_i(0) - \hat{\varphi}_0(0) = \mathcal{C}(\vartheta - \vartheta_{\mathrm{eq}}) \qquad \text{for } i = 1,2,3, \tag{22}$$

where ϑ_{eq} denotes the equilibrium temperature $\vartheta_{\mathrm{eq}} = 400\mathrm{K}$, see [15]. The constant $\mathcal{C} = 5.4\,\mathrm{MPa/K}$ depicts the Clausius-Clapeyron slope and has been taken from [18].
Finally, the approximated overall potential $\tilde{\Phi}^{(\mathrm{C})}$ is taken as the minimum of all local approximations:

$$\tilde{\Phi}^{(\mathrm{C})}(y,\vartheta) = \int_\Omega \min_i \Big(\frac{1}{2} \sum_{klmn} \mathbb{C}^i_{klmn} \varepsilon^i_{kl} \varepsilon^i_{mn} - \delta_{i0} \mathcal{C}(\vartheta - \vartheta_{\mathrm{eq}}) \Big)\, \mathrm{d}x. \tag{23}$$

4.2 Application: Two-way Micro-actuator

The approximated potential $\tilde{\Phi}^{(\mathrm{C})}$ from (23) can now be used for numerical simulations. As an example, we consider a two-way micro-actuator made of $Ni_{64}Al_{36}$. Such actuators are an important tool in the field of nano-engineering. These small components are used to generate forces or to cause small movements and thus form the active part within micro-scale and nano-scale devices. The area of application is very broad and rapidly increasing and includes micro-valves, nano-pliers etc. The advantage of SMA-based actuators compared to other techniques is their precision and reproducibility due to the fixed lattice structures.

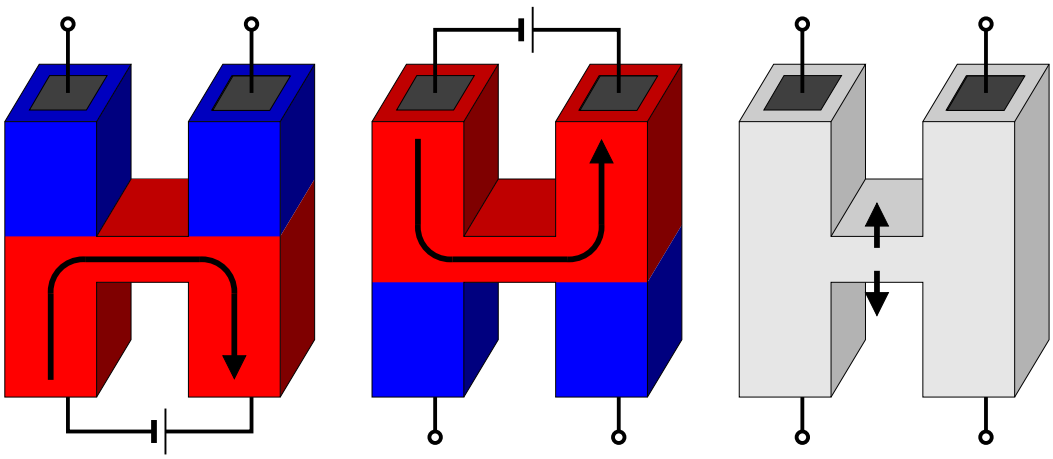

Figure 2: Operating principle of the two-way micro-actuator.

Two-way actuators are characterized by their ability to perform a certain movement forward and backward by themselves, i.e. the process is reversible. In contrast to this, one-way actuators can only perform a certain movement in one direction, whereas the return movement has to be induced by outer forces or the like.
The geometry of the two-way micro-actuator we consider here is shaped like the letter H. It is fixed at all four end points such that it is slightly stretched in vertical direction. To all four end points electrodes are attached. The impression of an electrical voltage to two of these electrodes causes a current to flow through a part of the actuator. As a consequence, parts of the device will be heated.
The operating principle is depicted in Figure 2. First, an electrical voltage is impressed to the lower two electrodes. This induces a current through the lower part of the actuator, including the bridge in the middle. This part is now heated, whereas the remaining part stays cold. This is depicted in red and blue in the left part of Figure 2. As a consequence, the specimen transforms to the austenite phase in the lower part, because this phase is energetically preferable at high temperatures. Opposed to this, the upper part exists in the martensitic phase. Due to the tensile stress in vertical direction, the upper part consists of the martensitic variant with the elongation in vertical direction, cf. Table 1. Thus the two upper rods of the actuator are slightly longer and thinner than the lower ones.
Then the process is reversed. The electrical current is turned off at the lower part and turned on at the upper part. Therefore the upper and the middle part will be heated, whereas the lower part cools down, see the second diagram of Figure 2. The upper part now transforms to the austenitic phase and the lower part to the martensitic phase. For the same reason as above, the two upper rods of the actuator are shortened and the lower ones lengthened. Since the whole actuator is fixed at the ends, the bridge in the middle of the actuator undergoes a vertical movement. This movement can be used for any desired purpose within the micro-device, such as to control a valve or the like.
The behavior of the actuator will now be simulated numerically. The time evolution is governed by the equation

$$\rho \frac{\partial^2 y}{\partial t^2} = \operatorname{div} \varphi'(\nabla y) \qquad \text{in } \Omega, \tag{24}$$

where $\rho = |\det A|^{-1} m$ denotes the mass density. The domain Ω is meshed by means of a simplicial grid. For our geometry here, 159.744 simplices have been used in total. The evolution equation (24) is then discretized in space using piecewise linear and globally continuous finite elements on this grid.
The time discretization is done using finite differences and an implicit scheme. The resulting discrete problem is then reformulated as a non-convex incremental minimization problem in terms of the potential energy. In each time step, it is solved by a steepest descent minimization routine with an Armijo time-step control. Due to the relatively slow transformation process, the mass ρ can be neglected. All numerical details can be found in [1].
The process of redirecting the electrical current is repeated several times within the simulation. After any

redirection, the temperature increases linearly in one part and decreases linearly in the other part. This is reflected in the model by setting the temperature ϑ accordingly and affects the offset of the different wells in the potential energy, cf. (23). The middle part is kept continuously hot due to the constant electrical current here.

The results of the numerical simulation are shown in Figure 3. First, the current is applied to the lower part. This leads to a transition to the austenitic phase, which is indicated by the green color. The upper part occurs in the martensitic variant which is elongated in vertical direction and displayed in yellow. The remaining two martensitic variants are plotted in red and blue. Then the current is altered. As a consequence, the upper rods transform to the austenite, whereas the lower ones transform to the martensite. This is depicted in the second and third snapshot. One can clearly observe the typical microstructure in the martensitic phase here. The fourth snapshot shows the fully finished transformation process. Note that the the middle bar moved upwards during the transformation. Then the current is altered again. The resulting reverse transformation is shown in the fifth and sixth snapshot.

References

[1] M. Arndt. *Multiscale Atomistic-Continuum Simulation of Shape-Memory Alloys*. PhD thesis, Institute for Numerical Simulation, University of Bonn, 2004. In preparation.

[2] M. Arndt and M. Griebel. Derivation of higher order gradient continuum models from atomistic models for crystalline solids. *Multiscale Model. Simul.*, 2004. Submitted.

[3] M. Arndt and M. Griebel. Higher order gradient continuum description of atomistic models for crystalline solids. In P. Neittaanmäki et al., editors, *Proceedings of the Fourth European Congress on Computational Methods in Applied Sciences and Engineering, Jyväskylä, Finland*, 2004.

[4] X. Blanc, C. Le Bris, and P.-L. Lions. From molecular models to continuum mechanics. *Arch. Ration. Mech. Anal.*, 164(4):341–381, 2002.

[5] E. Clementi and C. Roetti. Roothaan–Hartree–Fock atomic wavefunctions. *Atomic Data and Nuclear Data Tables*, 14:177–478, 1974.

[6] M. A. Collins. A quasicontinuum approximation for solitons in an atomic chain. *Chem. Phys. Lett.*, 77(2):342–347, 1981.

[7] M. S. Daw and M. I. Baskes. Embedded-atom method: Derivation and application to impurities, surfaces, and other defects in metals. *Phys. Rev. B*, 29(12):6443–6453, 1984.

[8] W. E and B. Engquist. The heterogeneous multi-scale methods. *Comm. Math. Sci.*, 1(1):87–133, 2003.

[9] W. E and Z. Huang. A dynamic atomistic-continuum method for the simulation of crystalline materials. *J. Comput. Phys.*, 182(1):234–261, 2002.

[10] P. Hohenberg and W. Kohn. Inhomogeneous electron gas. *Phys. Rev. B*, 136(3):864–871, 1964.

[11] K. Kadau. *Molekulardynamik-Simulationen von strukturellen Phasenumwandlungen in Festkörpern, Nanopartikeln und ultradünnen Filmen*. PhD thesis, Gerhard-Mercator-Universität Duisburg, 2001.

[12] M. D. Kruskal and N. J. Zabusky. Stroboscopic perturbation procedure for treating a class of nonlinear wave equations. *J. Math. Phys.*, 5(2):231–244, 1964.

[13] P. Rosenau. Dynamics of dense lattices. *Phys. Rev. B*, 36(11):5868–5876, 1987.

[14] P. Rosenau. Hamiltonian dynamics of dense chains and lattices: or how to correct the continuum. *Phys. Lett. A*, 311(1):39–52, 2003.

[15] S. Rubini and P. Ballone. Quasiharmonic and molecular-dynamics study of the martensitic transformation in Ni–Al alloys. *Phys. Rev. B*, 48(1):99–111, 1993.

[16] D. Schryvers, P. Boullay, R. V. Kohn, and J. M. Ball. Lattice deformations at martensite-martensite interfaces in Ni-Al. *J. Phys. IV*, 11(Pr8):23–30, 2001.

[17] E. B. Tadmor, M. Ortiz, and R. Phillips. Quasicontinuum analysis of defects in solids. *Philos. Mag. A*, 73(6):1529–1563, 1996.

[18] P. Šittner and V. Novák. Anisotropy of martensitic transformations in modeling of shape memory alloy polycrystals. *Int. J. Plast.*, 16(10-11):1243–1268, 2000.

[19] G. J. Wagner and W. K. Liu. Coupling of atomistic and continuum simulations using a bridging scale decomposition. *J. Comput. Phys.*, 190(1):249–274, 2003.

[20] N. J. Zabusky and M. D. Kruskal. Interaction of "solitons" in a collisionless plasma and the recurrence of initial states. *Phys. Rev. Lett.*, 15(6):240–243, 1965.

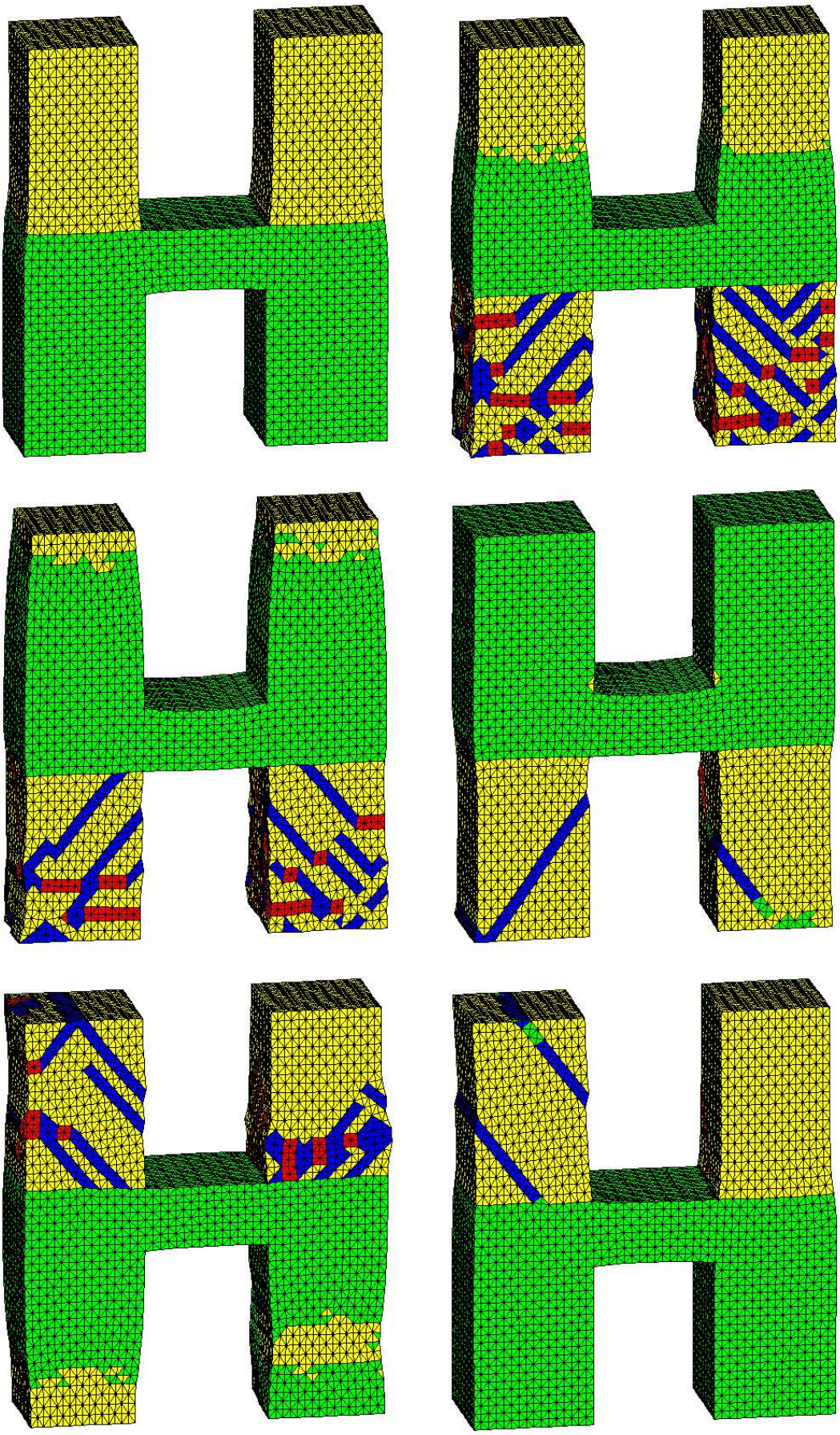

Figure 3: Snapshots of the continuum mechanical simulation of the two-way micro-actuator.